A Journal of the Gesellschaft Deutscher Chemiker

Angewandte International Edition GDCh Chemie

www.angewandte.org

Accepted Article

Title: Mosaic CuI–CuII–InIII 2D Perovskites: Pressure-Dependence of the Intervalence Charge Transfer and a Mechanochemical Alloying Method

Authors: Jiayi Li, Roc Matheu, Feng Ke, Zhenxian Liu, Yu Lin, and Hemamala Karunadasa

To be cited as: *Angew. Chem. Int. Ed.* **2023**, e202300957

Link to VoR: https://doi.org/10.1002/anie.202300957

WILEY VCH

10.1002/anie.202300957

WILEY-VCH

RESEARCH ARTICLE

Mosaic Cu^{I}–Cu^{II}–In^{III} 2D Perovskites: Pressure-Dependence of the Intervalence Charge Transfer and a Mechanochemical Alloying Method

Jiayi Li,[a] Roc Matheu,[a,b] Feng Ke,[c,d] Zhenxian Liu,[e] Yu Lin,[c] and Hemamala I. Karunadasa*[a,c]

[a] J. Li, Dr. R. Matheu, Prof. H. I. Karunadasa
Department of Chemistry
Stanford University
Stanford, California 94305, United States
E-mail: hemamala@stanford.edu
[b] Dr. R. Matheu (Current address)
Institut de Recerca de Química Teòrica i Computacional
Departament de Química Inorgànica i Orgànica, Universitat de Barcelona
Barcelona, 08007, Spain
[c] Dr. F. Ke, Dr. Y. Lin, Prof. H. I. Karunadasa
Stanford Institute for Materials and Energy Sciences
SLAC National Accelerator Laboratory
Menlo Park, California 94025, United States
[d] Dr. F. Ke
Department of Geological Sciences
Stanford University
Stanford, CA 94305, United States
[e] Prof. Z. Liu
Department of Physics
University of Illinois at Chicago
Chicago, IL 60607, United States

Supporting information for this article is given via a link at the end of the document.

Abstract: The 2D perovskite $(BA)_4[Cu^{II}(Cu^{I}In^{III})_{0.5}]Cl_8$ ($\mathbf{1_{BA}}$; BA^+ = butylammonium) allows us to study the high-pressure structural, optical, and transport properties of a mixed-valence 2D perovskite. Compressing $\mathbf{1_{BA}}$ reduces the onset energy of $Cu^{I/II}$ intervalence charge transfer from 1.2 eV at ambient pressure to 0.2 eV at 21 GPa. The electronic conductivity of $\mathbf{1_{BA}}$ increases by 4 orders of magnitude upon compression to 20 GPa, when the activation energy for conduction decreases to 0.16 eV. In contrast, Cu^{II} perovskites achieve similar conductivity at ~50 GPa. The solution-state synthesis of these perovskites is complicated, with more undesirable side products likely from the precursor mixtures containing three different metals. To circumvent this problem, we demonstrate an efficient mechanochemical synthesis to expand this family of halide perovskites with complex composition by simply pulverizing together powders of 2D Cu^{II} single perovskites and $Cu^{I}In^{III}$ double perovskites.

Introduction

Halide perovskites offer a rich diversity of electronic structures, mostly dictated by the inorganic framework of corner-sharing metal-halide octahedra. These octahedral sites commonly contain up to two different stoichiometric metal ions. We recently found that 2D halide perovskites can hold three stoichiometric metals in the octahedral sites through the synthesis of $R_4[Cu^{II}(Cu^{I}In^{III})_{0.5}]Cl_8$ ($\mathbf{1_R}$; R^+ = organoammonium; Figure 1 C).[1] This perovskite can be considered as a 1:1 alloy of a 2D single perovskite ($R_2Cu^{II}Cl_4$, Figure 1A)[2] and a 2D double perovskite ($R_4Cu^{I}In^{III}Cl_8$, Figure 1B),[3] featuring a unique octahedral metal site, which is best modeled as 2:1:1 mixture of Cu^{II}:Cu^{I}:In^{III}. We previously proposed a tiling model that explains how this ratio of Cu^{II}, Cu^{I}, and In^{III} coordination spheres can tile to fill 2D space (Figure 1D).[1] Since this tile can be translated/rotated, we refer to these complex compositions as "mosaic" perovskites to emphasize their different possible local arrangements. The coexistence of Cu^{I} and Cu^{II} and the resulting intervalence charge transfer (IVCT) in **1** afford new properties not seen in the parent 2D Cu^{II} or $Cu^{I}In^{III}$ perovskites. For example, **1** is opaque black with higher conductivity compared to its parent structures, which are colorless/yellow insulators. Because charge delocalization in mixed-valence compounds becomes more facile as the two metal centers show similar local coordination,[4,5] we sought to investigate the high-pressure properties of **1**. We are not aware of prior high-pressure studies of mixed-valence 2D perovskites. Further, since the high-pressure properties of 2D single[6–8] and double perovskites[9] have been intensely investigated, we sought to probe the effects of compression on more complex perovskites, featuring three distinct octahedral metal ions. Motivated by the new properties that arise in perovskites containing 3 distinct metal ions at the octahedral sites, we further demonstrate a mechanochemical synthetic method to expand this family of perovskites with multiple metals and oxidation states.

Results and Discussion

Mixed-valence halide perovskites

10.1002/anie.202300957
WILEY-VCH

RESEARCH ARTICLE

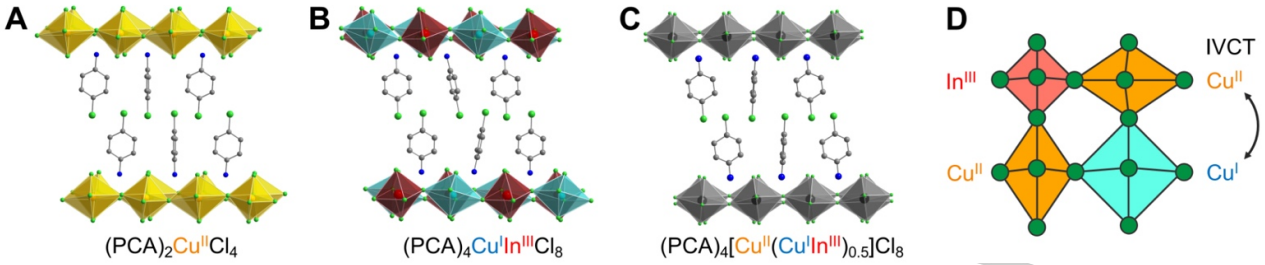

Figure 1. Single-crystal X-ray structures of (A) the 2D perovskite $(PCA)_2Cu^{II}Cl_4$,[2] (B) the 2D double perovskite $(PCA)_4Cu^{I}In^{III}Cl_8$,[3] and (C) the mosaic perovskite $(PCA)_4[Cu^{II}(Cu^{I}In^{III})_{0.5}]Cl_8$ (**1**$_{PCA}$);[1] PCA = *p*-chloroanilinium. Here, Cu^{II}–Cl, Cu^{I}–Cl, and In^{III}–Cl octahedra are shaded in yellow, turquoise, and dark red, respectively, whereas mixed $Cu^{II}/Cu^{I}/In^{III}$–Cl octahedra are shaded in gray. Green, blue, and gray spheres represent Cl, N, and C atoms, respectively, H atoms are not shown for clarity. (D) The proposed tile, which can be tessellated to fill the 2D sheet of the mosaic perovskite, **1**$_R$. The arrow indicates intervalence charge transfer (IVCT) between adjacent $Cu^{I/II}$ centers.

IVCT leads to intense optical absorption and enhanced electronic conductivity in a range of materials. More exotic phenomena, such as high-temperature superconductivity, have also been linked to mixed-valence in oxide perovskites, such as the $Cu^{I/II}$ or $Cu^{II/III}$ cuprates[10,11] and $Bi^{III/V}$ bismuthates.[12,13] Recently, their halide congeners, have received renewed attention due to their compositional tunability, low-temperature syntheses, and optoelectronic properties suitable for solar-cell and light-emitting applications.[14–16] However, mixed-valence halide perovskites are limited to only a few examples.[1,17–21] Halide perovskites are more compressible than their oxide analogs, with bulk moduli that are ca. an order of magnitude lower.[22] High-pressure studies of 3D halide perovskites have revealed increased conductivity and even metallization, albeit at very high pressures (e.g., 60 GPa).[6,7,22,23] The intensely studied mixed-valence halide double perovskite $Cs_2Au^{I}Au^{III}X_6$ (X = Cl, Br, I), originally synthesized in 1922,[24] shows metallic transport properties at a much lower pressure of 4.5 GPa for X = I.[25,26] A metallic phase has been proposed for the heavily disordered $Cs_2In^{I}In^{III}Cl_6$ at pressures above 22 GPa, based on Raman and optical absorbance measurements.[27] Although $Cs_2Tl^{I}Tl^{III}X_6$ has been predicted[28] to become a superconductor at high pressures with sufficient doping, this has yet to be experimentally realized.[14] Besides **1**$_R$, to our knowledge, the only other example of a mixed-valence 2D perovskite is $R_2(Au^{I}I_2)(Au^{III}I_4)(I_3)_2$ (R = organodiammonium) containing both halide (I^-) and pseudohalide (I_3^-) ligands.[29]

High-pressure studies of the mosaic perovskite: 1$_{BA}$

We initially measured powder X-ray diffraction (PXRD) patterns for $(BA)_4[Cu^{II}(Cu^{I}In^{III})_{0.5}]Cl_8$ (**1**$_{BA}$, BA: butylammonium) upon compression in a diamond-anvil cell (DAC) (Figure 2A). For all studies, the DAC was loaded under Ar to prevent Cu(I) oxidation and the pressure points were determined using a ruby scale.[30] The *α*-phase reflections shifted to higher angles up to 1.2 GPa, where the emergence of new reflections indicated an *α*-to-*β* phase transition. Based on observed reflections and systematic absences, we indexed the high-pressure *β* phase to the *P2/m* space group, although other assignments may be possible. Upon further compression, the *β*-phase reflections continuously shifted to higher angles up to 17 GPa. Above that pressure, some reflections shifted to lower angles, indicating a lattice expansion in the *c* axis (*β*-to-*γ* phase transformation). A lattice expansion upon material compression is unexpected. However, the terminal ammoniums typically nestle between adjacent octahedra in the inorganic framework, forming hydrogen bonds with both terminal and bridging halides.[31] Therefore, this *c*-axis expansion may be explained through a possible extrusion of the BA molecules away from the inorganic sheets as the sheets get more compressed. At higher pressures, the peak broadening in the PXRD patterns prevented the indexing of the *γ* phase. Upon decompression from 20 GPa to ambient pressure, the PXRD pattern matched that of the *α* phase and recovered the sharp peaks (Figure S16), indicating that the pressure-induced structural changes are reversible.

We extracted the unit-cell parameters through Rietveld (*α* phase) and Pawley refinements (*β* phase) of the PXRD patterns and fitted the parameters to a second-order Birch−Murnaghan equation of state (Figure 2B, Figure S17, Table S4–S5).[32] The bulk modulus

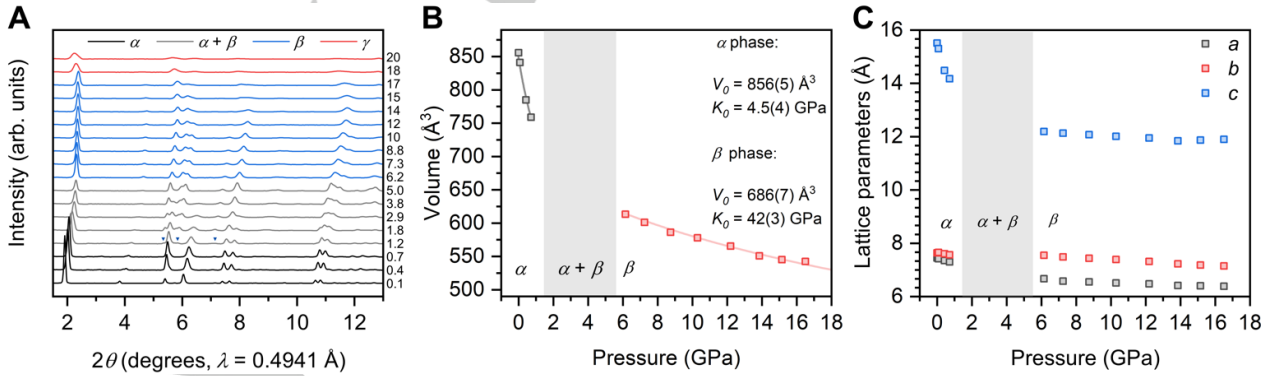

Figure 2. (A) PXRD patterns for **1**$_{BA}$ upon compression (without a pressure medium). Pressure ranges for each phase: *α* (0.1–0.7 GPa), *α* + *β* (1.2–5.0 GPa), *β* (6.2–17 GPa), and *γ* (18–20 GPa). The blue triangles indicate emerging reflections. (B) Unit-cell volume changes upon compression. The fits for the second-order Birch−Murnaghan equation of state are shown as lines, and their parameters are given for the *α* and *β* phases of **1**$_{BA}$. (C) Evolution of the lattice parameters of **1**$_{BA}$ as a function of pressure.

10.1002/anie.202300957

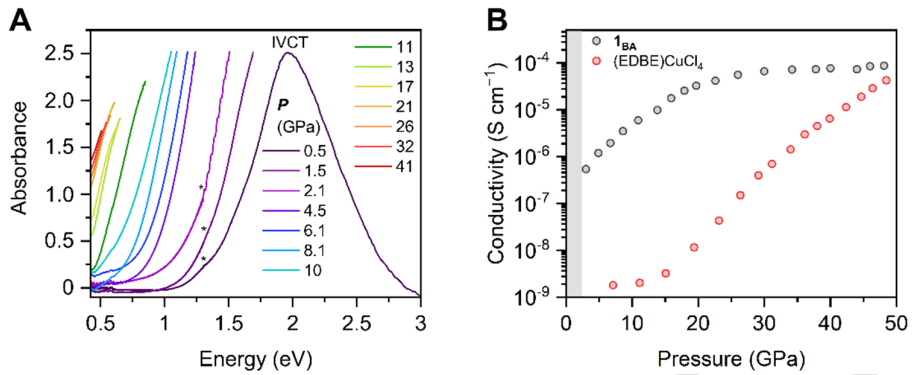

Figure 3. (A) Variable-pressure optical absorption spectra for $\mathbf{1}_{BA}$, showing a redshift of the intervalence charge-transfer (IVCT) band with increasing pressure. Asterisks indicate a detector change. (B) Electronic conductivity of $\mathbf{1}_{BA}$ as a function of pressure, compared with that of the 2D perovskite (EDBE)$CuCl_4$ (EDBE = 2,2′-(ethylenedioxy)bis(ethylammonium)).

of the *α* phase (K_0 = 4.5(4) GPa) reveals that this phase is much more compressible than the comparable 2D Cu^{II} perovskite R_2CuCl_4 (K_0 = 8.4 GPa for R^+ = ethylammonium and K_0 = 7.1 GPa for R^+ = propylammonium).[33] Most compression in the *α* phase occurs along the *c* axis, corresponding to a reduction of the interlayer distance, likely through increased interdigitation of the organic bilayers (Figure 2C). Notably, the K_0 for $\mathbf{1}_{BA}$ is one of the smallest values observed for halide perovskites.[22] In contrast, the bulk modulus of the *β* phase of $\mathbf{1}_{BA}$ (K_0 = 42(3) GPa) is comparable to that of the high-pressure phases of 2D Cu–Cl perovskites at a similar pressure range (K_0 = 22–60 GPa).[6,33,34] The unit-cell parameters of the *β* phase show a more isotropic compression of the three axes (Figure 2C) with pressure. We then tracked the structural changes of $\mathbf{1}_{BA}$ up to 40 GPa in a DAC containing Ne as a pressure-transmitting medium. The PXRD patterns of the *γ* phase (>20 GPa) were almost unvaried upon compression (Figure S18), suggesting a very stiff *γ* phase with little structural change in the 20–40 GPa pressure range.

At 1.7 GPa, the $\mathbf{1}_{BA}$ Raman spectrum exhibits two peaks at 163 and 259 cm^{-1} (Figure S19), similar to those reported for Cu^{II}–Cl (170 cm^{-1}) and In^{III}–Cl (280 cm^{-1}) bond stretching frequencies. The peaks shifted to higher energy and broadened upon compression (without a pressure medium), becoming almost indistinguishable from the background above 30 GPa. The peak assigned to In–Cl splits at 7 GPa, probably due to the *α*-to-*β* phase transition.

We then tracked the optical properties of $\mathbf{1}_{BA}$ up to ~40 GPa by measuring absorption spectra across the visible and near/mid-infrared wavelengths (using KCl as the pressure medium). At 0.5 GPa, the $\mathbf{1}_{BA}$ spectrum shows a band centered at 1.96 eV, consistent with the lowest-energy band observed at ambient pressure (Figure 3A). The IVCT transition likely dominates the band because d-d transitions are weak (Laporte forbidden) and thus not usually observed in transmission measurements.[1] Further, the low-energy region of the spectra (600–4000 cm^{-1}) contains IR signals related to the C–N, C–H and N–H bonds of the BA cation, matching the ambient-pressure IR spectrum of $\mathbf{1}_{BA}$ (Figure S21). We could not track the ligand-to-metal charge transfer (LMCT) band upon compression because it occurred at energies beyond the instrument detection limit in the lower-pressure range, and the IVCT band saturated the detector in the higher-pressure range. With increasing pressure, the onset of the IVCT band redshifted from ~1.2 eV (0.5 GPa) to ~0.2 eV (21 GPa) and remained almost constant upon further compression (Figure 3A). The redshifted IVCT band indicates that electron transfer between $Cu^{I/II}$ centers is becoming more facile, as the metal coordination spheres become more similar and come closer together with increasing pressure.[36,37] At higher pressures (>20 GPa), when the stiffer higher-pressure phase of $\mathbf{1}_{BA}$ does not show significant changes in the PXRD patterns indicating reduced structural changes, the optical absorption also remains mostly constant.

Motivated by the pressure-induced pronounced redshift of the IVCT band below 20 GPa, we measured four-point conductivities (*σ*) for $\mathbf{1}_{BA}$ powder upon compression under air-free conditions without a pressure medium (Figure 3B). The conductivity showed a strong pressure response, with a value of 5.4×10^{-7} S cm^{-1} at 3.0 GPa (close to the onset of the *β* phase), and reaching 3.2×10^{-5} S cm^{-1} at 20 GPa, representing a 10^4-fold increase compared to the ambient-pressure value for a single crystal.[1] Like the pressure-independent IVCT band above 20 GPa, the conductivity of $\mathbf{1}_{BA}$ remained mostly unchanged upon further compression. Variable-temperature conductivity gives activation energies (E_a) of 0.16 eV (20 GPa), and 0.11 eV (40 GPa), based on Arrhenius fits to the data (Figure S22). The high-pressure E_as are significantly lower than the ambient-pressure E_a (ca. 0.6 eV).[1] Hush et al. predicted a 4:1 ratio between the IVCT band maximum energy (E_{op}) and E_a for symmetrical one-electron transfer.[36] Although detector saturation prevents locating IVCT band maxima at most pressures, the theoretical E_{op} values (0.6 eV at 20 GPa and 0.4 eV at 40 GPa, calculated from $E_{op} = 4\times E_a$) are consistent with extrapolations of the optical absorption onsets using the spectra in the mid-IR region (Figure S24; ~0.2 eV at 20 GPa and ~0.15 eV at 40 GPa). Notably, the conductivity of $\mathbf{1}_{BA}$ (3.2×10^{-5} S cm^{-1}) at 20 GPa significantly exceeds the high-pressure conductivity of the single-valence 2D perovskite (EDBE)$CuCl_4$ (~10^{-8} S cm^{-1} at ~20 GPa). Indeed, (EDBE)$CuCl_4$ does not reach comparable conductivities until 49 GPa (Figure 3B).[6]

Mechanochemical alloying of single and double 2D perovskites

Encouraged by the pressure-induced transport in $\mathbf{1}_{BA}$, we sought ways to further tune the IVCT energy. However, likely due to the presence of three different metal ions in the solution-state assembly reactions, we could neither incorporate bromide into **1** due to competing side phases nor could we obtain phase-pure **1** with organoammonium cations other than BA. We therefore envisioned that a solid-state route may circumvent these

10.1002/anie.202300957

RESEARCH ARTICLE

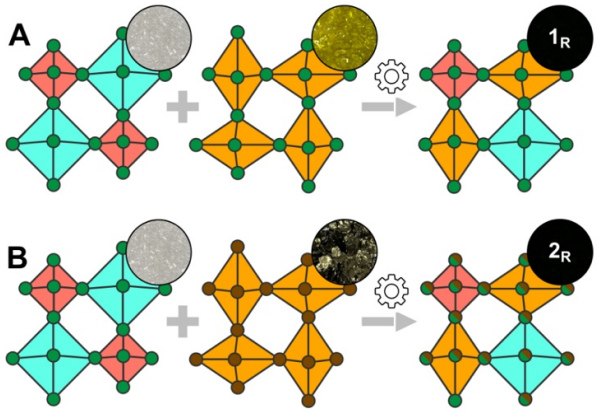

Figure 4. Mechanochemical synthesis of (A) $R_4[Cu^{II}(Cu^{I}In^{III})_{0.5}]Cl_8$ (**1**$_R$; R^+ = BA, PCA, and PEA; black powder) from R_2CuCl_8 (yellow powder) and $R_4CuInCl_8$ (colorless powder) and (B) $R_4[Cu^{II}(Cu^{I}In^{III})_{0.5}]Cl_4Br_4$ (**2**$_R$; R^+ = PCA and PEA; black powder) from R_2CuBr_4 (dark purple powder) and $R_4CuInCl_8$. Circular insets show the color of the perovskites. Red, turquoise, and orange quadrilaterals represent In^{III}, Cu^{I}, and Cu^{II} coordination spheres, respectively. Green and brown circles represent Cl and Br atoms, respectively.

problems.[38,39] Therefore, we first attempted the mechanochemical synthesis of **1**$_{BA}$ by ball-milling a 1:1 mixture of yellow $(BA)_2Cu^{II}Cl_4$ and colorless $(BA)_2(Cu^{I}In^{III})_{0.5}Cl_4$ powders using inert ZrO_2 balls under air-free conditions. The color of the mixture drastically changed from yellow to black upon ball-milling (Figure 4A). PXRD data unambiguously confirmed the conversion of the precursor single and double perovskites to the mosaic perovskite (Figure S2). We then combined 2D $R_2Cu^{II}Cl_4$ or $R_2Cu^{II}Br_4$ single perovskites and 2D $R_2(Cu^{I}In^{III})_{0.5}Cl_4$ double perovskites to form the chloride mosaic perovskites: $R_4[Cu^{II}(Cu^{I}In^{III})_{0.5}]Cl_8$ (R^+ = PCA (**1**$_{PCA}$) or PEA (**1**$_{PEA}$); Figure 4A) and the mixed-halide mosaic perovskites: $R_4[Cu^{II}(Cu^{I}In^{III})_{0.5}]Cl_4Br_4$ (R^+ = PCA (**2**$_{PCA}$) or PEA (**2**$_{PEA}$); Figure 4B). PXRD patterns of the products indicate complete conversion to the mosaic perovskites after ball-milling (Figure S3–S7) and the phase purity was further confirmed by Le Bail refinement of PXRD data and CHN elemental analysis (Supporting Information). The integrity of the organic cations and different metal-ligand stretching modes were probed by infrared spectroscopy (Figures S13–S15) and Raman spectroscopy (Figure S9–S11, Table S3), respectively. Notably, this is the first phase-pure synthesis for **1**$_{PCA}$, **1**$_{PEA}$, **2**$_{PCA}$, and **2**$_{PEA}$, although crystals of **1**$_{PCA}$ and **1**$_{PEA}$ were previously separated from a mixture of phases crystallized from solution.[1]

Although mechanochemical syntheses typically start with simple precursors (metal halides and organoammonium salts),[38] the solid-state milling of the 3D perovskites $(CH_3NH_3)PbCl_3$ and $(CH_3NH_3)PbBr_3$ has been reported to mix the halides.[40] To our knowledge, 2D perovskites of different composition have not previously been mechanically alloyed. Intriguingly, ball-milling did not result in the delamination and restacking of the precursor 2D perovskite sheets, despite the weak interactions between the organic bilayers that enable exfoliation.[41] As seen in certain 2D double perovskites, X-ray diffraction data alone cannot distinguish between a disordered distribution of metals within a single inorganic layer and a lack of registry between different layers, such that the average structure appears to have metal disorder.[42,43] Instead, the $Cu^{I/II}$ IVCT—which is not expected occur across the organic bilayer—indicates an intimate mixing of the three metals, even within a single perovskite sheet.

Tuning the $Cu^{I/II}$ IVCT through the ligand

We compared the optical properties of **1** and **2** to gauge the effects of halide substitution. Consistent with their black color, the diffuse reflectance spectra of **1**$_{PEA}$, **1**$_{PCA}$, **2**$_{PEA}$, and **2**$_{PCA}$ obtained under air-free conditions exhibit strong absorption across the entire visible region, displaying two features centered at ~1.3–1.8 eV and ~2.7–3.2 eV (Figure 5A and S12). By comparing with the diffuse reflectance spectra of Cu^{II} perovskites (Figure S12), we assigned the higher-energy transitions of **1** and **2** (2.7–3.2 eV) to ligand-to-metal charge transfer (LMCT), whereas the lower-energy bands (1.3–1.8 eV) correspond to a combination of d-d transitions and IVCT bands (Figure 5B). The mixed-halide perovskites exhibit a redshift in both bands compared to the chloride perovskites. Bromide substitution redshifts the LMCT band for the mosaic perovskites with PEA and PCA, by ca. 0.60 eV, as expected due to the higher energy Br 4p orbitals compared the Cl 3p orbitals.[44] The d-d transitions of 2D Cu^{II} perovskites are less sensitive to the halide due to the metal-centered nature of the

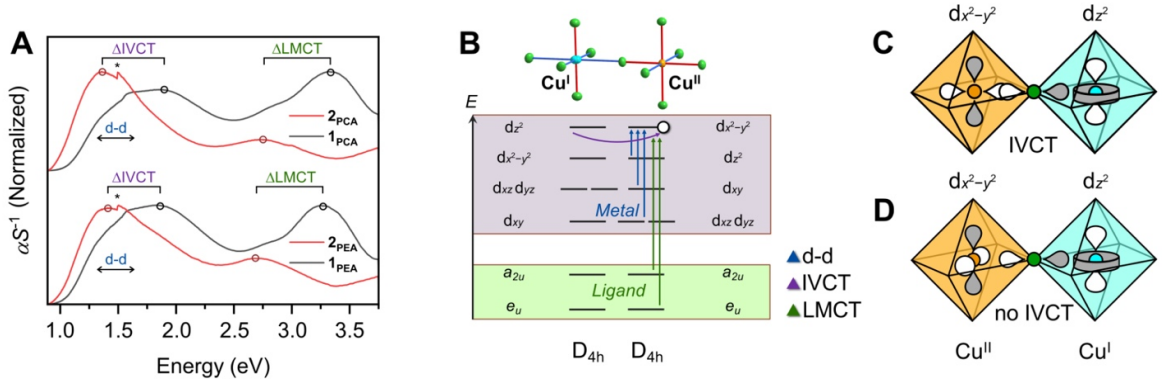

Figure 5. (A) Diffuse reflectance spectra for **1**$_R$ and **2**$_R$ (R = PCA, PEA). The diffuse reflectance data were transformed using the Kubelka–Munk function (α and S are the pseudo-absorption and scattering coefficients, respectively). Asterisks indicate a detector change. (B) Illustrations of the three types of electronic transitions in **1**$_R$ and **2**$_R$: d-to-d transitions (blue), ligand-to-metal charge transfer (LMCT, green), and intervalence charge transfer (IVCT, purple). The d orbitals are named using local coordinates, where the unique axis is the z axis. The blue and red bonds represent elongated and compressed Cu–Cl bonds, respectively. (C) The proposed tilling model for mosaic perovskites, where the elongated Cu^{II}-Cl bonds do not connect to the Cu^{I} center. The molecular orbitals formed with Cl 3p orbitals and the Cu^{I} dz^2 orbitals/Cu^{II} dx^2–y^2 orbitals allow for the IVCT. (D) A hypothetical model of $Cu^{I/II}$ centers, where the elongated Cu^{II}–Cl bonds connect to the Cu^{I} center. Facile IVCT is not possible due to the orthogonal arrangement of the Cu^{I} dz^2 and Cu^{II} dx^2–y^2 orbitals. The Cu^{II} and Cu^{I} octahedral sites are shaded in orange and turquoise, respectively.

transitions (Figures 5B and S12A). Therefore, although these bands are obscured by the IVCT transition in 1 and 2, we expect a similarly small energy shift. Estimations of the IVCT peak maxima show that bromide alloying redshifts the peak by ca. 0.48 and 0.42 eV for the PCA and PEA derivatives, respectively (Figure 5A).

The $Cu^{I/II}$ IVCT and the proposed tiling model

A closer look at the orbitals involved in the IVCT further bolsters the tiling model proposed for the mosaic perovskites (Figure 1D). The Cu^{I} center in $R_4Cu^{I}In^{III}Cl_8$ exhibits an axial contraction typical of d^{10} metals, and also seen in 2D double perovskites with Ag^{I},[45] which is attributed to mixing between filled *n*d orbitals and empty (*n*+1)s orbitals, resulting in the stabilization of a linear geometry.[46] Likewise, the Cu^{II} centers in R_2CuCl_4 show the well-known axial elongation mediated by the Jahn-Teller distortion of the d^9 metal. These different bond lengths are maintained in the alloy, **1**, as evidenced by the bond lengths and thermal ellipsoids in the single-crystal X-ray structure solutions.[1] Thus, the IVCT occurs between the Cu^{I} dz^2 orbital and Cu^{II} $dx^2–y^2$ orbital (Figure 5B). Although these two orbitals lie along orthogonal axes, the distinct packing arrangement in the alloyed perovskite changes the local and global unique axes: the contraction of the Cu^{I} octahedron only occurs perpendicular to the inorganic sheet, whereas the elongation of the Cu^{II} octahedron only occurs parallel to the inorganic sheet. Thus, charge transfer is allowed between the Cu^{I} dz^2 HOMO and the Cu^{II} $dx^2–y^2$ SOMO through the bridging Cl. Notably, only the short bonds of Cu^{II} contact the Cu^{I} in our proposed tiling unit (Figure 5C), and this is the only arrangement that allows for the IVCT. If the elongated Cu^{II}-Cl bonds connect to the Cu^{I}, the orbitals involved in IVCT would indeed be almost orthogonal (Figure 5D), since octahedral tilting is minor. Thus, not only does the In^{III} allow for Cu^{I} and Cu^{II} to be incorporated into a 2D perovskite, but it also facilitates the correct orientation of molecular orbitals that enables IVCT within a single tile.

Conclusion

The mosaic perovskites allow us to access adjacent $Cu^{I/II}$ sites, which otherwise does not occur in stoichiometric layered perovskites. The mixed-valence 2D perovskites exhibit appreciable conductivity at moderate pressures through facile IVCT upon compression. At 20 GPa, the high-pressure conductivity of $\mathbf{1_{BA}}$ is 3.2×10^{-5} S cm^{-1}; Cu^{II} perovskites do not reach comparable conductivity until ca. 50 GPa.[6] We further demonstrate how to expand this perovskite family by simply pulverizing together solid Cu^{II} and Cu^{I}-In^{III} perovskites with various halides and organoammoniums. We expect that this mechanochemical alloying will be a general method to target various mosaic perovskites, in a simple, solvent-free method to circumvent the many side phases possible in solution-state syntheses, especially for more complex compositions. These perovskites may set the stage for studying $M^{I/II}$, $M^{I/III}$, $M^{II/III}$, and $M^{I/II/III}$ (M = metal) mixed-valence in halide perovskites.

Acknowledgements

The high-pressure work was supported by the Department of Energy (DOE), Office of Basic Energy Sciences (BES), Division of Materials Sciences and Engineering (DE-AC02-76SF00515) and the mechanochemical synthesis was supported by the National Science Foundation (DMR2102306). J.L. was supported by the Stanford Interdisciplinary Graduate Fellowship. SC-XRD studies were performed at the Stanford Nano Shared Facilities (SNSF), supported by the National Science Foundation under award ECCS-1542152. High-pressure PXRD patterns were collected at beamline 12.2.2 at the Advanced Light Source, supported by the Office of Science, BES, DOE (DE-AC02-05CH11231). High-pressure absorption measurements used beamline 22-IR-1 of the National Synchrotron Light Source II, a U.S. DOE Office of Science User Facility operated by the Brookhaven National Laboratory (DE-SC0012704) and supported by COMPRES under the National Science Foundation (EAR 11-57758) and the Carnegie DOE Alliance Center (DE-FC03-03N00144). We thank Dr. Martin Kunz for the technical assistance and Prof. Wendy Mao for access to equipment.

Keywords: high pressure • conductivity • intervalence charge transfer • mechanochemical synthesis • 2D perovskite

References

[1] B. A. Connor, R. W. Smaha, J. Li, A. Gold, A. J. Heyer, F. Toney, Y. S. Lee, H. I. Karunadasa, *Chem. Sci.* **2021**, *12*, 8689–8697.
[2] A. K. Vishwakarma, P. S. Ghalsasi, A. Navamoney, Y. Lan, A. K. Powell, *Polyhedron* **2011**, *30*, 1565–1570.
[3] Deposition number 2205650 (for $(PCA)_4Cu^{I}In^{III}Cl_8$) contains the supplementary crystallographic data for this paper. The data are provided free of charge by the Cambridge Crystallographic Data Centre.
[4] H. Tanino, K. Syassen, Z. Wang, M. Hanfland, K. Takahashi, *High Pressure Research* **1990**, *3*, 183–185.
[5] M. B. Robin, P. Day, in *Advances in Inorganic Chemistry and Radiochemistry* (Eds.: H.J. Emeléus, A.G. Sharpe), Academic Press, **1968**, pp. 247–422.
[6] A. Jaffe, Y. Lin, W. L. Mao, H. I. Karunadasa, *J. Am. Chem. Soc.* **2015**, *137*, 1673–1678.
[7] A. Jaffe, S. A. Mack, Y. Lin, W. L. Mao, J. B. Neaton, H. I. Karunadasa, *Angew. Chem. Int. Ed.* **2020**, *132*, 4046–4051.
[8] H. Li, Y. Qin, B. Shan, Y. Shen, F. Ersan, E. Soignard, C. Ataca, S. Tongay, *Adv. Mater.* **2020**, *32*, 1907364.
[9] Y. Fang, L. Zhang, L. Wu, J. Yan, Y. Lin, K. Wang, W. L. Mao, B. Zou, *Angew. Chem. Int. Ed.* **2019**, *58*, 15249–15253.
[10] N. P. Armitage, P. Fournier, R. L. Greene, *Rev. Mod. Phys.* **2010**, *82*, 2421–2487.
[11] C. W. Chu, L. Z. Deng, B. Lv, *Physica C: Superconductivity and its Applications* **2015**, *514*, 290–313.
[12] A. W. Sleight, J. L. Gillson, P. E. Bierstedt, *Solid State Commun.* **1975**, *17*, 27–28.
[13] R. J. Cava, B. Batlogg, J. J. Krajewski, R. Farrow, L. W. Rupp, A. E. White, K. Short, W. F. Peck, T. Kometani, *Nature* **1988**, *332*, 814–816.
[14] G. E. Eperon, M. T. Hörantner, H. J. Snaith, *Nat. Rev. Chem.* **2017**, *1*, 1–18.
[15] M. D. Smith, B. A. Connor, H. I. Karunadasa, *Chem. Rev.* **2019**, *119*, 3104–3139.
[16] Q. A. Akkerman, G. Rainò, M. V. Kovalenko, L. Manna, *Nat. Mater.* **2018**, *17*, 394–405.
[17] M. Retuerto, T. Emge, J. Hadermann, P. W. Stephens, M. R. Li, Z. P. Yin, M. Croft, A. Ignatov, S. J. Zhang, Z. Yuan, C. Jin, J. W. Simonson, M. C. Aronson, A. Pan, D. N. Basov, G. Kotliar, M. Greenblatt, *Chem. Mater.* **2013**, *25*, 4071–4079.
[18] L. Atkinson, P. Day, *Journal of the Chemical Society A: Inorganic, Physical, Theoretical* **1969**, 2423–2431.
[19] J. Bill, K. Lerch, W. Laqua, *Zeitschrift für anorganische und allgemeine Chemie* **1990**, *589*, 7–11.
[20] N. Kojima, H. Kitagawa, *J. Chem. Soc., Dalton Trans.* **1994**, 327–331.
[21] X. Tan, P. W. Stephens, M. Hendrickx, J. Hadermann, C. U. Segre, M. Croft, C.-J. Kang, Z. Deng, S. H. Lapidus, S. W. Kim, C. Jin, G. Kotliar, M. Greenblatt, *Chem. Mater.* **2019**, *31*, 1981–1989.
[22] A. Jaffe, Y. Lin, H. I. Karunadasa, *ACS Energy Lett.* **2017**, *2*, 1549–1555.

10.1002/anie.202300957

[23] R. Matheu, F. Ke, A. Breidenbach, N. R. Wolf, Y. Lee, Z. Liu, L. Leppert, Y. Lin, H. I. Karunadasa, *Angew. Chem. Int. Ed.* **2022**, *61*, e202202911.
[24] H. L. Wells, *Am. J. Sci.* **1922**, *s5-3*, 315–326.
[25] N. Kojima, H. Kitagawa, T. Ban, F. Amita, M. Nakahara, *Solid State Commun.* **1990**, *73*, 743–745.
[26] S. Wang, A. F. Kemper, M. Baldini, M. C. Shapiro, S. C. Riggs, Z. Zhao, Z. Liu, T. P. Devereaux, T. H. Geballe, I. R. Fisher, W. L. Mao, *Phys. Rev. B* **2014**, *89*, 245109.
[27] J. Lin, H. Chen, Y. Gao, Y. Cai, J. Jin, A. S. Etman, J. Kang, T. Lei, Z. Lin, M. C. Folgueras, L. N. Quan, Q. Kong, M. Sherburne, M. Asta, J. Sun, M. F. Toney, J. Wu, P. Yang, *Proc. Natl. Acad. Sci.* **2019**, *116*, 23404–23409.
[28] Z. P. Yin, G. Kotliar, *EPL* **2013**, *101*, 27002.
[29] L. M. Castro-Castro, A. M. Guloy, *Angew. Chem. Int. Ed.* **2003**, *42*, 2771–2774.
[30] H. K. Mao, P. M. Bell, J. W. Shaner, D. J. Steinberg, *J. Appl. Phys.* **1978**, *49*, 3276–3283.
[31] B. Saparov, D. B. Mitzi, *Chem. Rev.* **2016**, *116*, 4558–4596.
[32] F. Birch, *Phys. Rev.* **1947**, *71*, 809–824.
[33] F. Aguado, F. Rodríguez, R. Valiente, J.-P. Itiè, M. Hanfland, *Phys. Rev. B* **2012**, *85*, 100101.
[34] Q. Li, S. Li, K. Wang, Z. Quan, Y. Meng, B. Zou, *J. Phys. Chem. Lett.* **2017**, *8*, 500–506.
[35] P. Han, W. Zhou, D. Zheng, X. Zhang, C. Li, Q. Kong, S. Yang, R. Lu, K. Han, *Adv. Opt. Mater.* **2022**, *10*, 2101344.
[36] N. S. Hush, in *Progress in Inorganic Chemistry*, John Wiley & Sons, Ltd, **1967**, pp. 391–444.
[37] D. M. D'Alessandro, F. Richard Keene, *Chem. Soc. Rev.* **2006**, *35*, 424–440.
[38] F. Palazon, Y. E. Ajjouri, H. J. Bolink, *Adv. Energy Mater.* **2020**, *10*, 1902499.
[39] A. D. Jodlowski, A. Yépez, R. Luque, L. Camacho, G. de Miguel, *Angew. Chem. Int. Ed.* **2016**, *55*, 14972–14977.
[40] A. Karmakar, A. M. Askar, G. M. Bernard, V. V. Terskikh, M. Ha, S. Patel, K. Shankar, V. K. Michaelis, *Chem. Mater.* **2018**, *30*, 2309–2321.
[41] A. G. Ricciardulli, S. Yang, J. H. Smet, M. Saliba, *Nat. Mater.* **2021**, *20*, 1325–1336.
[42] M. K. Jana, S. M. Janke, D. J. Dirkes, S. Dovletgeldi, C. Liu, X. Qin, K. Gundogdu, W. You, V. Blum, D. B. Mitzi, *J. Am. Chem. Soc.* **2019**, *141*, 7955–7964.
[43] E. T. McClure, A. P. McCormick, P. M. Woodward, *Inorg. Chem.* **2020**, *59*, 6010–6017.
[44] R. Matheu, J. A. Vigil, E. J. Crace, H. I. Karunadasa, *Trends Chem.* **2022**, *4*, 206–219.
[45] B. A. Connor, L. Leppert, M. D. Smith, J. B. Neaton, H. I. Karunadasa, *J. Am. Chem. Soc.* **2018**, *140*, 5235–5240.
[46] I. B. Bersuker, *Chem. Rev.* **2013**, *113*, 1351–1390.

10.1002/anie.202300957

WILEY-VCH

RESEARCH ARTICLE

Entry for the Table of Contents

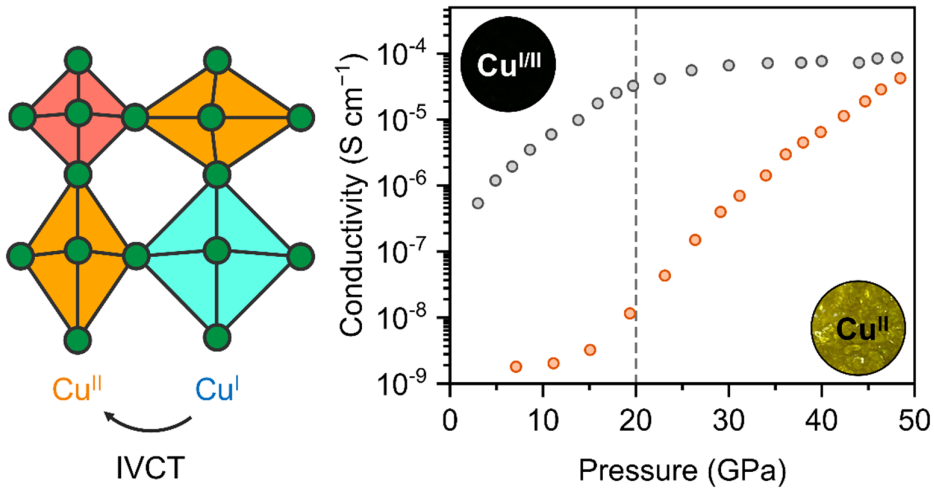

The mosaic perovskites, featuring 3 different octahedral metal sites, allow for adjacent $Cu^{I/II}$ sites, which otherwise does not occur in stoichiometric layered perovskites. The $Cu^{I/II}$ intervalence charge transfer (IVCT) affords a 30-GPa reduction in the onset pressure for appreciable conductivity (10^{-5} S cm^{-1}) compared to a Cu^{II} perovskite.